Atmospheric
Measurement
Techniques
Discussions

1   # EVALUATION OF UV AEROSOL RETRIEVALS FROM AN OZONE LIDAR

2   Shi Kuang[1]*, Bo Wang[1], Michael J. Newchurch[1], Paula Tucker[1], Edwin W. Eloranta[2], Joseph P.

3   Garcia[2], Ilya Razenkov[2], John T. Sullivan[3], Timothy A. Berkoff[4], Guillaume Gronoff[4,5], Liqiao

4   Lei[4,6], Christoph J. Senff[7,8], Andrew O. Langford[7], Thierry Leblanc[9], Vijay Natraj[10]

5   [1]University of Alabama in Huntsville, Huntsville, Alabama, USA

6   [2]University of Wisconsin-Madison, Madison, Wisconsin, USA

7   [3]NASA Goddard Space Flight Center, Greenbelt, Maryland, USA

8   [4]NASA Langley Research Center, Hampton, Virginia, USA

9   [5]Science Systems and Applications Inc., Lanham, Maryland, USA

10   [6]Universities Space Research Association, Columbia, Maryland, USA

11   [7]NOAA Earth System Research Laboratory, Boulder, Colorado, USA

12   [8]Cooperative Institute for Research in Environmental Sciences, University of Colorado, Boulder, Colorado, USA

13   [9]Jet Propulsion Laboratory, California Institute of Technology, Wrightwood, CA, USA

14   [10]Jet Propulsion Laboratory, California Institute of Technology, Pasadena, California, USA

15

16   *Correspondence to: Shi Kuang (kuang@nsstc.uah.edu)

17

18   **Abstract**

19   Aerosol retrieval using ozone lidars in the ultraviolet (UV) band is challenging but necessary for correcting aerosol

20   interference in ozone retrieval and for studying the ozone-aerosol correlations. This study describes the aerosol

21   retrieval algorithm for a tropospheric ozone lidar, quantifies the retrieval error budget, and intercompares the aerosol

22   retrieval products at 299 nm with those at 532 nm from a high spectral resolution lidar (HSRL). After the cloud-

23   contaminated data is filtered out, the aerosol backscatter or extinction coefficients at a 30-m and 10-min resolution

24   retrieved by the ozone lidar are highly correlated with the HSRL products, with a coefficient of 0.95 suggesting that

25   the ozone lidar can reliably measure aerosol structures with high spatio-temporal resolution when the signal-to-noise

26   ratio is sufficient. The actual uncertainties of the aerosol retrieval from the ozone lidar generally agree with our

27   theoretical analysis. The backscatter color ratio (backscatter-related exponent of wavelength dependence) linking the

28   coincident data measured by the two instruments at 299 and 532 nm is 1.34±0.11 while the Ångström (extinction-

29   related) exponent is 1.49±0.16 for a mixture of urban and fire smoke aerosols within the troposphere above Huntsville,

30   AL, USA.

31   **1.   Introduction**

32   A tropospheric ozone differential absorption lidar (DIAL) makes measurements of vertical ozone profiles, typically

33   at two wavelengths chosen between 277 and 300 nm with a separation less than 12 nm, by weighing several parameters

34   such as the ozone absorption cross sections, solar background, dynamic range of the detection system, and interference

35   from aerosols and other species (e.g., Alvarez et al., 2011; De Young et al., 2017; Fukuchi et al., 2001; Kempfer et

36   al., 1994; McDermid et al., 2002; Proffitt and Langford, 1997; Strawbridge et al., 2018; Sullivan et al., 2014). Vertical

37   aerosol profiles are of high interest not only because they are needed for aerosol correction in ozone lidar retrievals,

38   but also because simultaneous ozone and aerosol vertical profile measurements provide unique information on their

39   interactions and sources of pollutant transport (Browell et al., 1994; Newell et al., 1999). However, there is currently

40   no consensus on the reliability of the aerosol retrievals produced by ozone lidars due to the difficulty of solving the

41   three-component lidar equation and the large variability in aerosol optical properties associated with the multiplicity

42   of aerosol types and size distributions.

43   The most widely used solution for the elastic single-wavelength aerosol lidar equation is the analytic method

44   developed by Klett (1981). The inversion method then inspired Fernald (1984) to publish a computer algorithm scheme

45   to solve the more general two-component (aerosol and molecular) atmospheric lidar equation. The Klett (1981)

46   inversion requires *a priori* for the lidar ratio (i.e., aerosol extinction-to-backscatter ratio, represented by "S" thereafter)

47   to link the aerosol backscatter with its extinction for solving the lidar equation. Lasers used for aerosol lidars are

48   preferred in the visible and infrared bands, typically 532 or 1064 nm, where the ozone absorption is negligible

49   compared to molecular and Mie scattering. In the UV band for an ozone lidar, the ozone absorption may not be trivial.

50   Some ozone lidars have an aerosol channel available, either independently or sharing receiving optics with the ozone

51   channel (e.g., Browell et al., 1994; De Young et al., 2017; Gronoff et al., 2019; Kovalev and McElroy, 1994; Uchino

52   and Tabata, 1991). For most of the traditional two-wavelength ozone lidars without an aerosol channel, although the

53   aerosol retrieval algorithm has been discussed in a few literatures (e.g., Eisele and Trickl, 2005; Langford et al., 2019;

54   Papayannis et al., 1999; Sullivan et al., 2014), the evaluation of the aerosol retrieval product and its error budget have

55   rarely been addressed. Due to a significant wavelength difference with aerosol lidars, several aspects of the aerosol

56   retrieval using an ozone lidar are worth noting. Firstly, the signal-to-noise ratio (SNR) for ozone lidars decays quicker

57   with altitude due to more significant UV molecular (i.e., Rayleigh) scattering and ozone absorption resulting in a lower

58   retrievable altitude than aerosol lidars. Secondly, because the molecular and ozone components become more

59   important for a UV wavelength compared to visible and infrared wavelengths, the uncertainties in aerosol retrieval

60   propagated from the calculation of these two components are expected to be larger for an ozone lidar than aerosol

61   lidars. Thirdly, S and the wavelength dependence used for the ozone lidar wavelengths may be different from those

62   used for the longer aerosol lidar wavelengths (Ackermann 1998; Eck et al., 1999).

63   The primary objectives of this article are to investigate the performance of our aerosol retrieval algorithm

64   and quantify its error budget for the ozone lidar. The secondary goal is to seek the overall wavelength dependence

65   between the aerosol optical properties measured by the ozone lidar at 299 nm and by a high spectral resolution lidar

66   (HSRL) at 532 nm.

67   **2.   Instruments and Data Processing**

68   **2.1.   Ozone Lidar**

69   The Rocket-city Ozone (O_3) Quality Evaluation in the Troposphere (RO_3QET) lidar is located on the campus of the

70   University of Alabama in Huntsville (UAH) at 34.725 °N and 86.645 °W at 206 m asl and is one of the six systems of

71   the Tropospheric Ozone Lidar Network (TOLNet) (http://www-air.larc.nasa.gov/missions/TOLNet). This system

72   measures ozone from 0.1 km up to about 12 km during nighttime and up to about 6 km during daytime with a temporal

73   resolution of 2 min. The vertical resolution of the lidar retrievals varies from 150 m in the lower troposphere to 750

74   m in the upper troposphere in order to keep the measurement uncertainty within ±10% (Kuang et al., 2013).

75   The transmitter comprises two Raman-shifted lasers at 289 and 299 nm. Two 30-Hz, 266-nm Nd:YAG lasers

76   pump two 1.8-m Raman cells, respectively, with mixtures of active gas and buffer gas to generate 289 and 299-nm

77   lasers with an average pulse energy of about 5 mJ. The receiving system consists of three receivers with diameters of

78   2.5 cm, 10 cm, and 40 cm, respectively, and four photomultipliers (PMTs) similar to that described by Kuang et al.

79   (2013) except that the solar filters have been replaced by 300-nm short-pass filters for all telescopes. Channels -1, 2,

80   3, 4 represent the 2.5-cm, 10% of the 10-cm, 90% of the 10-cm, and the 40-cm telescope channels, respectively. Since

81   the modification of Channel-4 through the addition of narrow-band solar filters was not completed before the time

82   period of this study, data from this channel was not used in this work, resulting in that the uncertainties for ozone

83   retrievals above 6 km during daytime were often too large due to strong solar background. Lidar signal counting was

84   accomplished by four Licel transient recorders (Licel company, Germany) with both analog and photoncounting (PC)

85   modes, with a sampling rate of 40 MHz corresponding to a 3.75-m fundamental resolution. Derivatives of the off-line

86   analog signal serve to label clouds by setting an appropriate threshold. The cloud filtering process should be conducted

87   carefully because an elastic lidar without a polarization channel is not capable of accurately distinguishing aerosols

88   and clouds solely by their backscatter properties. Therefore, the data with clouds lower than 2 km was discarded. Five

89   2-min lidar data intervals were combined to give a 10-min lidar-signal integration time to improve the SNR. Further,

90   six of the 3.75-m fundamental bins were integrated for all channels. In addition, dead-time correction (for PC signal

91   only), background correction, analog-PC signal merging, and signal-induced noise correction were performed.

92   **2.2.   Introduction of the Aerosol Retrieval Algorithm and Uncertainty Estimation**

93   The aerosol profiles were retrieved with an iterative DIAL algorithm. A brief description of this algorithm is

94   provided in this section, with further details in Appendix A. A first-order Savitzky-Golay differentiation filter with a

95   second-degree polynomial was applied to the logarithm of the signal ratios to compute the first-cut ozone profile. This

96   initial ozone profile was substituted back into the three-component lidar equation to derive the profile of aerosol

97   backscatter coefficients at 299 nm by assuming a constant S of 60 sr and boundary value of the aerosol backscatter

98   coefficient at a far-range reference altitude, about 10 km. During the daytime, the ozone retrieval was limited by the

99   lower SNR of the 289-nm channel, but the 299-nm channel had much better SNR due to lower atmospheric extinction

100   and was able to measure aerosol up to higher altitudes. S is highly variable with aerosol characteristics, humidity, and

101   wavelength (Ackermann, 1998; Strawbridge et al., 2018; Mishchenko et al., 1997). The S *a priori* value assumed for

102   this study represents a mix of urban and smoke aerosols during the lidar observations (Ackermann, 1998; Burton et

103   al., 2012; Cattrall et al., 2005; Groß et al., 2013; Müller et al., 2007). The *a priori* is application dependent. In the

104   aerosol retrieval uncertainty discussion in Appendix B, we assume a ±20% uncertainty for S based on an average

105   standard deviation obtained from prior observations (Müller et al., 2007).

106   Molecular backscatter and extinction profiles were computed from local radiosonde data. Then, the aerosol

107   profile was substituted into the lidar equation again to obtain a stable solution, usually within three iterations. This

108   aerosol profile was further employed to calculate the aerosol correction for ozone retrievals using the first-order Taylor

109   approximation (Browell et al., 1985) by assuming a power law wavelength dependence for the aerosol extinction and

Atmospheric
Measurement
Techniques
Discussions

110   choosing an appropriate Ångström exponent. Since this paper focuses only on aerosol retrieval, details of the ozone

111   correction will be described in a future article. Finally, the aerosol profiles derived by the three altitude channels were

112   merged to a single profile in the overlapping altitude zones, i.e., 0.5–1 km for Channels 1 and 2 and 1.5–2 km for

113   Channels 2 and 3.

114   The primary uncertainty sources for the aerosol lidar retrievals are the uncertainties in lidar signal

115   measurement, boundary value assumption for aerosol backscatter coefficient, air density measurement, S *a priori*, and

116   ozone profile input. The relative importance of these sources are altitude dependent. In the planetary boundary layer

117   (PBL) where the air is typically turbid, the S uncertainty is dominant while other sources are minor (only few percent).

118   The uncertainty of S influences the uncertainty of the aerosol backscatter through a complicated relationship. However,

119   the magnitude of the above two uncertainties can be approximately seen to be close. At the far range (higher than 7

120   km), lidar signal detection noise and inaccurate boundary value assumption are important. Influence from both of the

121   above sources, especially the boundary value, on the aerosol retrieval quickly decreases as you go towards the ground

122   from the far range. In the middle range (PBL top – 7 km), both the air density measurement error and lidar signal

123   detection noise are essential. Uncertainty due to ozone profile input is relatively unimportant and is only few percent

124   at most altitudes. Figure B1 presents an example of the aerosol backscatter uncertainty calculated from 10-min

125   nighttime RO3QET lidar data. The error budget estimate generally justifies the choice of using 6 km as the maximum

126   altitude for RO3QET-HSRL comparison since the total uncertainty for the RO3QET aerosol retrieval could be

127   unacceptably large (i.e., persistently larger than 100%).

128   **2.3.   HSRL**

129   The University of Wisconsin HSRL (Eloranta, 2005) was deployed in Huntsville, AL from 19 June to 4 November

130   2013 and operated almost 24 hours every day to support the Studies of Emissions and Atmospheric Composition,

131   Clouds and Climate Coupling by Regional Surveys SEAC[4]RS campaign (Kuang et al., 2017). The HSRL transmitter

132   was a diode-pumped Nd:YAG laser at 532 nm with a pulse energy of about 50 μJ and a pulse repetition frequency of

133   4 kHz. The expanded laser beam was transmitted coaxially with a 40-cm telescope with a tiny field of view of 100

134   μrad to reduce solar background. The HSRL spectral filtering can separate the molecular backscatter from the aerosol

135   backscatter due to the molecular Doppler broadening effect while the particulate backscatter remains spectrally

136   unbroadened. Aerosol backscatter coefficients can then be calculated as the difference between the total return and

137   the molecular component (Grund and Eloranta, 1991). We intercompare the backscatter coefficients measured by the

138   two instruments to avoid the extra uncertainty due to the S assumption for the HSRL. The HSRL provides aerosol

139   products with a 30-m vertical resolution and 1-min temporal resolution from near the surface to 15 km. To achieve

140   sufficient SNR for both HSRL and ozone lidar and to reduce the uncertainty arising from the clock bias of the

141   controlling computers, we adopt 10-min temporal average and 30-m spatial average for both HSRL and ozone lidar

142   in the intercomparison study. The HSRL has a backscatter measurement precision better than 10^{-7} (m sr)$^{-1}$ for a 1-min

143   signal average (Reid et al., 2017), which represents an estimated precision for the extinction coefficient of better than

144   2×10^{-6} m^{-1} for a 10-min average.

145   **3.   Intercomparison Results**

146   We select four time periods 21–23 June, 14–15 August, 27–28 August, and 5–6 September 2013 to investigate the

147   ozone lidar capability for measuring aerosol column and range-resolved profiles. All four cases have coincident ozone

148   lidar and HSRL observation periods longer than 24 hours, fully covering the convective mixing layer development

149   and collapse processes (Klein et al., 2019) and having significant smoke layers in the free troposphere. Due to the

150   significant extinction and potential multiple scattering caused by clouds, the ozone lidar is incapable of measuring

151   either ozone or aerosol accurately above clouds, especially thick clouds. Therefore, data contaminated by clouds is

152   filtered out. At this time, the narrow-band interference filters had not been incorporated into the receiving system and

153   the wide-band filter resulted in substantial solar background during the daytime; hence, we set 6 km asl as the

154   maximum altitude for intercomparison. The uncertainty of the aerosol retrieval owning to lidar signal measurement

155   error is dominant at far range and is determined by lidar SNR as shown in Appendix B.2. The solar background is an

156   important noise resulting in the lidar signal measurement error during daytime and is partly responsible for the high

157   aerosol retrieval uncertainty above 6 km as shown by the example in Figure B1. The 10-min HSRL profiles are

158   interpolated to the times of the ozone lidar data.

159   First, we investigate the correlation of the integrated (or column) aerosol backscatter between the ozone lidar

160   and HSRL to obtain a general relationship between their averages. Figure 1 shows that the RO$_3$QET- and HSRL-

161   derived integrated backscatter coefficients for all four cases are highly correlated, with a Pearson correlation

162   coefficient of 0.99. The 493 sampling profiles cover 82 hours of coincident ozone lidar and HSRL observations. We

163   define the aerosol backscatter color ratio ($\mathring{a}_\beta$) as (Burton et al., 2012):

164
$$\mathring{a}_\beta = -\frac{d(ln\beta_A)}{d(ln\lambda)} = -\frac{ln\left(\frac{\beta_A^{299}}{\beta_A^{532}}\right)}{ln\left(\frac{299}{532}\right)}, \tag{1}$$

165   where β_A^{299} and β_A^{532} represent the aerosol backscatter coefficient at 299 and 532 nm, respectively. The subscript "A"

166   represents the "aerosol" component to be distinguished with the "molecular" contribution which is represented by

167   subscript "M" in the Appendix. $\mathring{a}_\beta$ is an exponent denoting backscatter-related wavelength dependence, to be

168   distinguished from the commonly-used Ångström exponent (Ångström, 1929) that refers to the wavelength

169   dependence of optical thickness or extinction coefficient. $\mathring{a}_\beta$ is also different from another often-used concept, "color

170   ratio of the lidar ratios" which refers to the ratio of S at two different wavelengths. The slope of the regression (2.16)

171   results in the best least-square fit value of 1.34 for $\mathring{a}_\beta$ at 299 and 532 nm. The uncertainty of the column β_A^{299} is

172   expected to be smaller than the uncertainty for β_A^{299} at a particular altitude and for a 10-min integration time (in Figure

173   B1) since the average over longer time and altitude range greatly reduces the random noise. If the uncertainty of the

174   column β_A^{299} measurements is estimated to be 20% which is primarily due to the uncertainty of the S *a priori* (a

175   systematic error), we can estimate the corresponding uncertainty for $\mathring{a}_\beta$=1.34 to be ±0.11 by error propagation from

176   Eq. (1). $\mathring{a}_\beta$ has important applications in aerosol type classification from (spectral) aerosol lidar measurements (e.g.,

177   Cattrall et al., 2005; Hair et al., 2008; Müller et al., 2007). There is significant variation in $\mathring{a}_\beta$ for 532–1064 nm

178   reported in different studies, with numbers ranging from negative values to 2.3 (Burton et al., 2012; Cattrall et al.,

179   2005; Müller et al., 2007). However, all of these studies show $\mathring{a}_\beta$ for smoke and urban aerosols was larger than

180   maritime and dust aerosols. Since most previous studies report $å_\beta$ for wavelengths longer than 355 nm, $å_\beta$ calculated

181   in this study for 299–532 nm could provide valuable data for UV wavelengths.

182   In practice, aerosol extinction is a more meaningful parameter and more relevant for several applications than

183   backscatter. For the HSRL, the extinction coefficients are linearly converted from the backscatter coefficients by

184   assuming a constant S=55 sr with 20% uncertainty, in the same manner as Reid et al. (2017). The estimated Ångström

185   exponent for 299 and 532 nm is 1.49±0.16, using the data in Figure 1 after considering uncertainties in S for both

186   lidars. The Ångström exponent from this study (1.49±0.16) is within a reasonable range compared to previous studies.

187   For example, Ångström exponent was measured by Raman lidar to be between 1.35±0.2 and 1.56±0.2 at 355 nm for

188   smoke aerosols in Canada (Strawbridge et al., 2018). Ångström exponent for urban aerosols was measured to be

189   1.4±0.5 in Europe and 1.7±0.5 in North America for 355 and 532-nm wavelengths (Müller et al., 2007).

190   Figure 2 presents the intercomparison of the aerosol backscatter retrieved by the HSRL and the RO$_3$QET

191   lidar for the four cases in 2013. The HSRL-derived aerosol backscatter coefficients are scaled to 299 nm (represented

192   by "HSRL-converted" thereafter) using the best-fit exponent value $å_\beta$=1.34. Some clouds lower than 2 km show up

193   in the HSRL curtains but not in the RO$_3$QET curtains (e. g., 1500–2100 on 15 August and 1500–2100 on 28 August).

194   These low-cloud-contaminated data were discarded in the RO$_3$QET lidar pre-processing program because the

195   retrievable range was not long enough. The profiles with clouds higher than 2 km measured by the RO$_3$QET were

196   retained and the aerosol retrievals below the clouds were used for the range-resolving intercomparisons.

197   In terms of the aerosol measurement evaluation, we pay attention to the RO$_3$QET lidar's two capabilities:

198   measuring the PBL diurnal evolution and measuring free-tropospheric smoke layers. In Figure 2, the PBL heights

199   measured by the two lidars, which are identified by large aerosol gradients, are highly consistent for all cases. The

200   development of the convective mixing layer in the early morning, an important process responsible for surface ozone

201   increase, can be visually identified in most RO$_3$QET curtains (e.g., 1400–1700 UTC or 0900–1200 local time in Figure

202   2-h). The aerosol structures and evolutions in the free troposphere measured by the RO$_3$QET lidar are highly similar

203   to those measured by the HSRL. For example, the RO$_3$QET lidar captured an extremely thin aerosol layer ~5 km on

204   27–28 August (Figure 2-g), which probably originated from the Pacific Northwest fire and has been discussed by Reid

205   et al. (2017). The large aerosol uncertainties for the RO$_3$QET lidar at far ranges are consistent with expectation. As

206   demonstrated in Appendix B, aerosol retrieval uncertainties due to lidar signal measurement error and the boundary

207   value chosen at the reference altitude, two of the most important sources of uncertainty, increase with altitude and

208   may exceed 100% at ~7 km.

209   To evaluate the ozone lidar's range-resolving capability for aerosol retrieval, we intercompared the aerosol

210   backscatter coefficients, for all cases, from the two instruments with a 10-min temporal resolution and a 30-m vertical

211   resolution after filtering out cloud-contaminated data as shown in Figure 3. The high correlation coefficient of 0.95

212   suggests that the RO$_3$QET lidar can capture the aerosol variability with high spatio-temporal resolutions. The

213   correlation coefficient for the high vertical resolution retrievals is slightly less than that for the column average (0.99

214   in Figure 1) due to less average with respect to range.

215   Figure 4 presents the mean and 1-σ standard deviations of the relative differences between RO$_3$QET and

216   HSRL, (RO$_3$QET-HSRL)/HSRL, to be compared with the theoretical 1-σ error calculated as outlined in Appendix B.

217   The HSRL measurements are considered as the "true" values to be compared with the RO$_3$QET measurements. Both

218   the theoretical and actual 1-σ values generally increase with altitude. The actual differences between RO$_3$QET and

219   HSRL measurements are mostly within or comparable to the theoretical calculation of the RO$_3$QET measurement

220   uncertainties. The structures of the theoretical uncertainties are consistent with the actual differences at most altitudes,

221   with few exceptions. For example, the large discrepancies (red lines compared to blue lines in Figure 4) occurring at

222   ~4.5 km in Figure 4 (c) and ~1.5 km in Figure 4 (d) are primarily because of small number division effects for the

223   extremely clean atmospheric layers (also see Figure 2). Aerosol backscatter of clean air probably can be accurately

224   measured by the HSRL, but, may be beyond the measurement sensitivity of RO$_3$QET.

225   In Figure 4, the RO$_3$QET-measured aerosols are generally higher than the HSRL-measured aerosols between

226   5 and 6 km so that the RO$_3$QET-HSRL differences deflect to the right side with altitude. There were both clean air

227   and smoke layers between 5 and 6 km for the four cases; therefore, the positive differences cannot be explained solely

228   by the lower capability of RO$_3$QET for measuring clean air. We hypothesize that another reason causing these

229   differences is the underestimated backscatter color ratio for the smoke aerosols. We converted the HSRL backscatter

230   from 532 to 299 nm using a constant backscatter color ratio, 1.34, which represents an average for the column-

231   integrated backscatter. The most considerable contribution to integrated backscatter comes from PBL aerosols, which

232   are mostly urban aerosols with a lower backscatter color ratio than either fresh or aged smoke (Burton et al., 2012;

233   Cattrall et al., 2005). The uncertainty of the backscatter color ratio was not considered in the error budget of the aerosol

234   retrieval. In addition, we ignored the measurement uncertainty of the HSRL. Therefore, the general agreement of the

235   theoretical estimate of the aerosol retrieval uncertainties and the actual errors suggests that our analysis of the

236   uncertainty sources in Appendix B is reasonable.

237   **4. Conclusions**

238   We have evaluated the aerosol retrievals at 299 nm from the RO$_3$QET ozone lidar using aerosol retrievals at 532 nm

239   from the highly precise University of Wisconsin HSRL from the coincident observations at Huntsville, AL in 2013.

240   The integrated backscatter coefficients between 0.4 and 6 km asl (0.2 and 5.8 km agl) from the two instruments are

241   highly correlated, with a coefficient of 0.99 after excluding cloud-contaminated data. Since the ozone lidar is not able

242   to accurately measure either ozone or aerosol above clouds, cloud-contaminated data can significantly distort the

243   relationship between the products from the two instruments. The aerosol profiles of backscatter coefficients at 30-m

244   vertical and 10-min temporal resolution retrieved by the RO$_3$QET are also highly correlated with those from the HSRL

245   with a coefficient of 0.95 suggesting that the ozone lidar is capable of producing reliable aerosol structure information

246   at high spatio-temporal resolution. Intercomparison of the backscatter product was chosen to avoid additional

247   uncertainty caused by the lidar ratio (S) assumption needed for the HSRL aerosol extinction retrieval.

248   The aerosol retrieval algorithm and its error budget are shown in the Appendix. The primary uncertainty

249   sources for the aerosol lidar retrieval are errors in lidar signal measurement, boundary value assumption, air density

250   calculation, S *a priori*, and ozone profile input. The uncertainty in S assumption is a dominant source at near range

251   while the lidar signal measurement and boundary value errors dominate at far range, as shown in Figure B1 for an

252   example. Within the middle range (PBL top – about 7 km), the air density calculation error is essential and is larger

253   or comparable to the lidar signal measurement error. The total uncertainty generally increases with altitude from about

Atmospheric
Measurement
Techniques
Discussions

254   15% in the PBL to consistently higher than 100% above 7 km. Theoretical estimates of the error budget are generally

255   consistent with the RO$_3$QET-HSRL measurement differences.

256   By assuming a constant S of 60 sr for the ozone lidar, the backscatter coefficients measured by the two

257   instruments are related by a backscatter color ratio (backscatter-related exponent) of 1.34±0.11 for 299 and 532 nm.

258   The extinction-related Ångström exponent that is more relevant for various applications is estimated to be 1.49±0.16

259   by assuming S = 55 sr for the HSRL at 532 nm. These exponents represent a summertime average for a mixture of

260   urban pollution and fire smoke. We did not separate the aerosol types, although we understand that S and Ångström

261   exponent vary with the aerosol phase function and size distribution. The aerosol correction in the ozone lidar retrieval

262   will be described in a subsequent paper.

263

264   **Appendix A. Aerosol retrieval algorithm**

265   The ozone DIAL solution can be written as follows:

266    $$n_{(r)} = \frac{-1}{2\Delta\sigma} \times \frac{d}{dr}\left[ln\frac{P_{\text{on}(r)}}{P_{\text{off}(r)}}\right] + [B] + [E] \ , \qquad (A1)$$

267   where $n_{(r)}$ is the ozone number density at range r, $\Delta\sigma$ is the differential ozone absorption cross section, $P_{\text{on}(r)}$ and $P_{\text{off}(r)}$

268   are the backscattered on-line and off-line lidar returns, and $[B]$ and $[E]$ represent the differential backscatter and

269   extinction terms (Browell et al., 1985), respectively, including both molecular and aerosol components. The first term

270   of the right side of Eq. (A1) is often called the signal term. The subscripts "on" and "off" represent 289 and 299 nm

271   for this study. The aerosol extinction coefficients at 299 nm are calculated using the following procedure.

272   1)   A first-order Savitzky-Golay differentiation filter with a second-degree polynomial and variable fitting

273   window widths are applied on $ln\frac{P_{\text{on}(r)}}{P_{\text{off}(r)}}$ to compute the signal term. This smoothing method can accommodate the

274   rapid decay of the lidar signal with altitude to provide sufficient SNR for ozone retrievals by appropriate selection of

275   smoothing window widths (Leblanc et al., 2016a).

276   2)   By canceling the lidar constant using the two lidar equations at range r and $r+\Delta r$ for 299 nm, the aerosol

277   backscatter coefficients at range r can be expressed as:

278    $$\beta_A(r) = -\beta_M(r) + \frac{Z(r)}{Z(r+\Delta r)}[\beta_A(r + \Delta r) + \beta_M(r + \Delta r)]\exp\left\{-2\Delta r[\alpha_A\left(r + \frac{\Delta r}{2}\right) + \alpha_M\left(r + \frac{\Delta r}{2}\right) + \alpha_{O3}\left(r + \frac{\Delta r}{2}\right)]\right\} \ ,$$

279   (A2)

280   where $\beta_A(r)$ and $\beta_M(r)$ are aerosol and molecular backscatter coefficients at range r, respectively; $Z(r) = P_{\text{off}}r^2$ is

281   the range-corrected lidar signal at 299 nm; $\alpha_A(r+\Delta r/2)$, $\alpha_M(r+\Delta r/2)$, and $\alpha_{O3}(r+\Delta r/2)$ represent the average aerosol,

282   molecular, and ozone extinction coefficients between range r and $r+\Delta r$, respectively. Assuming the 299-nm lidar ratio,

283    $S=\alpha_A/\beta_A$, is constant with the range at 60 sr for this study and further assuming:

284    $$\alpha_A(r + \frac{\Delta r}{2}) \approx \alpha_A(r + \Delta r) = S\beta_A(r + \Delta r), \qquad (A3)$$

285   Eq. (A2) contains only two unknown variables: the aerosol backscatter coefficient $\beta_A(r+\Delta r)$ and ozone extinction

286   coefficient $\alpha_{O3}(r+\Delta r/2)$, which requires knowledge of the ozone number density $n_{(r+\Delta r/2)}$. Molecular backscatter and

287   extinction can be computed from nearby radiosonde data or a model with acceptable accuracy. For the first iteration

288   step, $n_{(r+\Delta r/2)}$ can be computed from the signal term in Eq. (A1). By assuming a start value β_A(ref) at a reference

289 range and a constant S with range, $\beta_A(r)$ can be solved by Equation (A2). Then, the first $\beta_A(r)$ profile is substituted

290 back into (A2) to compute the second estimate by using a more accurate form for $\alpha_A(r+\Delta r/2)$ as:

$$\alpha_A\left(r + \frac{\Delta r}{2}\right) = S[\beta_A(r + \Delta r) + \beta'_A(r)]/2, \tag{A4}$$

292 where $\beta'_A(r)$ represents the value from the first estimate. Typically, a stable solution for $\beta_A(r)$, which does not change

293 significantly from one iteration step to the next, can be obtained with only three iterations of Eq. (A2) and (A4.

294 3)   The correction terms, $[B]$ and $[E]$, in Eq. (A1) are calculated by the Browell et al. (1985) approximation,

295 assuming a power law dependence with wavelength for the aerosol extinction and choosing an appropriate Ångström

296 exponent. Since this paper focuses only on aerosol retrievals, the details of the ozone corrections will be described in

297 a future article.

298 4)   Aerosol profiles computed for the three altitude channels are finally merged to a single profile in their

299 overlapping altitude zones, 0.5–1 km for Channels 1 and 2, 1.5–2 km for Channels 2 and 3.

300

301 **Appendix B. Error budget of the aerosol retrieval**

302 Now we investigate five primary error sources affecting each term on the right side of Eq. (A2). In the following

303 section, we use the notation Δ to represent the absolute uncertainty and δ to represent the relative uncertainty. For a

304 function Y, derived from several measurement variables x_1, x_2, …, the uncertainty in Y can be estimated by the

305 following expression using the first-order Taylor expansion approximation when these variables are independent:

$$\Delta Y^2 = (\Delta x_1 \frac{\partial Y}{\partial x_1})^2 + (\Delta x_2 \frac{\partial Y}{\partial x_2})^2 + \cdots . \tag{B1}$$

307 **B.1 Lidar signal measurement error**

308 The error source to determine the normalized lidar signal ratio term $\frac{Z(r)}{Z(r+\Delta r)}$ is the lidar signal measurement error, ΔP.

309 Although ΔP may be due to various processes such as inaccurate dead-time correction, inaccurate background

310 subtraction, and signal-induced noise, its dominant component is the lidar signal statistical uncertainty (often called

311 lidar signal detection noise) and is typically assumed to obey a Poisson distribution. Assuming no error in deciding r,

312 by using Eq. (A2) and (B1) we obtain the uncertainty of the aerosol backscatter owing to lidar signal measurement

313 error relative to the total backscatter as:

$$\frac{\Delta\beta_A^{sig}(r)}{\beta_A(r)+\beta_M(r)} = \sqrt{[\delta P(r)]^2 + [\delta P(r + \Delta r)]^2}, \tag{B2}$$

315 where $P(r)$ represents lidar signal counts at r after omitting the wavelength subscript (i.e., 299 nm) and $\delta P(r)$ is just

316 the inverse of SNR. This means that the uncertainty of the aerosol backscatter coefficient due to lidar signal

317 measurement is determined by the lidar SNR similarly to other remote sensing detection techniques. Consequently,

318 its relative uncertainty can be written as:

$$\delta\beta_A^{sig}(r) = \left(\frac{1}{B(r)} + 1\right)\sqrt{[\delta P(r)]^2 + [\delta P(r + \Delta r)]^2}, \tag{B3}$$

320 where $B(r)=\beta_A(r)/\beta_M(r)$ is the aerosol-to-molecular backscatter ratio. As expected, $\delta\beta_A^{sig}(r)$ has a reverse relationship

321 with $\beta_A(r)$ since it is a relative uncertainty. Figure B1 shows an example of the uncertainty budget for a 10-min lidar

322 data profile. The aerosol retrieval uncertainty due to the lidar signal measurement error generally increases with

323 altitude primarily because of the rapidly decaying lidar SNR.

B.2 Boundary value error

According to Eq. (A2), the uncertainty of the aerosol backscatter at r, $\beta_A(r)$, can be induced by the uncertainty of the backscatter at $r + \Delta r$, $\beta_A(r + \Delta r)$, due to the iterative computation method. The error propagation between the adjacent altitudes can be determined by their partial differential relationship. Using the traditional far-end solution by assuming that the air is clean at a reference altitude, the aerosol uncertainty due to the inaccurate boundary value assumption propagates downward based on the following equation:

$$\delta\beta_A^{BV}(r) = \delta\beta_A(r + \Delta r) \left[\frac{1 + \frac{1}{B(r)}}{1 + \frac{1}{B(r+\Delta r)}} \right] \{ 1 - 2S\Delta r \beta_A(r + \Delta r)[1 + \frac{1}{B(r+\Delta r)}]\}. \tag{B4}$$

The yellow line in Figure B1 represents the relative uncertainty of backscatter retrieval due to the boundary value assumption, $\delta\beta_A^{BV}(r)$, when $\delta\beta_A(r_b) = 1000\%$ (i.e., 10 times overestimate at r_b =10 km). Despite a large overestimate at the reference altitude, $\delta\beta_A^{BV}(r)$ decreases toward the ground, to less than 10% below 5.5 km and less than 1% below 3.5 km. Simulations demonstrate that $\delta\beta_A^{BV}(r)$ for an underestimation of $\delta\beta_A(r_b)$ (not shown) is better than that for an overestimation, indicating that the boundary value is preferred at a smaller value. As suggested by Eq. (B4), $\delta\beta_A^{BV}(r)$ is affected by both S and B. Larger S (if it is correct) results in smaller $\delta\beta_A^{BV}(r)$ and, therefore, aerosol retrieval errors converge to zero faster. In other words, the smaller the value of S is, the more sensitive the aerosol retrieval is to the boundary value error. $\delta\beta_A^{BV}(r)$ decreases with an increase of $B(r)$. This means that $\delta\beta_A^{BV}(r)$ is less affected by the assumed value of $\beta_A(r_b)$ when the aerosol backscatter becomes more important relative to molecular backscatter, which occurs at longer wavelengths or under turbid air conditions. It is to be noted that $\delta\beta_A(r_b)$ is between -1 and $+\infty$ so that the distribution of $\delta\beta_A^{BV}(r)$ is asymmetric with the zero axis.

In terms of the influence of the boundary value error, we have compared our calculation with an analytical solution proposed by Kovalev and Moosmüller (1994) (not shown); the results are almost identical. Aerosol retrieval uncertainty due to incorrect boundary value assumption tends to converge to zero towards the lidar. It is negligible at lower altitudes, especially in the PBL, when the air is turbid.

B.3 Air density error

According to Eq. (A2), the air density profile affects $\beta_M(r)$, $\beta_M(r+\Delta r)$, and the optical depth (or transmittance). Similarly, we can derive the relative uncertainty in aerosol backscatter owing to the uncertainty in the air density profile as:

$\delta\beta^{AD}_A(r)$

$$= \sqrt{\{\frac{\delta\beta_M(r)}{B(r)}[1 + S_m\Delta r\beta_A(r) + S_m\Delta r\beta_M(r)]\}^2 + \{\frac{\delta\beta_M(r + \Delta r)\left[\frac{1}{B(r)} + 1\right]}{B(r + \Delta r) + 1}[1 - S_m\Delta r\beta_A(r + \Delta r) - S_m\Delta r\beta_M(r + \Delta r)]\}^2}$$

$. \tag{B5}$

S_m represents the molecular extinction-to-backscatter ratio, which is a constant ($8\pi/3$). The two parts in the square root are the components due to the uncertainties at r and $r+\Delta r$, respectively. Each component includes the influences from both molecular backscatter and optical depth. When Δr is small, the contribution of the optical depth error is much smaller than that of the molecular backscatter error so that (B4) can be approximated as:

$$\delta\beta^{AD}_A(r) \approx \sqrt{2}\frac{\delta\beta_M(r)}{B(r)}. \tag{B6}$$

358   It is to be noted that $\Delta\beta_M(r)$ and $\Delta\beta_M(r+\Delta r)$ are independent errors as assumed in Eq. (B1). If they are correlated, Eq.

359   (B5) will partly cancel out with their covariance term, which is not shown in (B1). Due to the nature of the iterative

360   computation method, $\delta\beta^{AD}_A(r + \Delta r)$ affects $\delta\beta^{AD}_A(r)$ as noted in Eq. (B4), so that the aerosol retrieval uncertainty due

361   to air density error will propagate downward. However, model simulation suggests that the systematic error of the air

362   density calculation has little impact on the aerosol retrieval because of the cancelation of the effect at r and $r + \Delta r$. Eq.

363   (B6) means the uncertainty in the calculation of molecular backscatter will mostly linearly propagate to aerosol

364   backscatter. If the 2-σ precision of a radiosonde is 0.3 K and 0.5 hPa for temperature and pressure measurements

365   (Hurst et al., 2011), the propagated uncertainty onto molecular backscatter is only about 0.1%. However, the real

366   disturbance of an atmosphere deviating from the actual air density profile may be more significant since there are

367   usually only a few radiosonde profiles available every day. Hence, we assume $\delta\beta_M(r)$ to be 1% and the resulting

368   aerosol retrieval uncertainty is represented by the green line in Figure B1. $\delta\beta^{AD}_A(r)$ can be tens of percent in the free

369   troposphere and is an important error source for aerosol retrievals (Russell et al., 1979). $\delta\beta^{AD}_A(r)$ is less than 10% in

370   the PBL because of more turbid air in that region. Since $\delta\beta_M(r)$ is assumed to be a constant in this example, the

371   variation of $\delta\beta^{AD}_A(r)$ is mostly a result of varying $B(r)$, the aerosol-to-molecular backscatter ratio. Since $B(r)$ generally

372   increases with an increase in wavelength, $\delta\beta^{AD}_A(r)$ is expected to be smaller at longer wavelengths. Therefore, the

373   aerosol retrieval is less sensitive to the air density error at longer wavelengths.

374   **B.4 Lidar ratio error**

375   By using Eqn. (A2) and (B1), the relative uncertainty in aerosol backscatter due to incorrect lidar ratio (*S*) assumption

376   can be calculated as follows:

377

378   $$\delta\beta^S_A(r) = 2\left[\frac{1}{B(r)} + 1\right]\Delta S\beta_A(r)\Delta r. \qquad (B7)$$

379   $\delta\beta^S_A(r)$ due to ΔS at only range r appears to be small, about 1%, when Δr is specified at 22.5 m. However, ΔS varying

380   with altitude is mostly systematic and, therefore, $\delta\beta^S_A(r)$ at every altitude will propagate downward and these effects

381   will accumulate. The error accumulation is not straightforward to compute as an analytical solution. However, these

382   effects can be simulated numerically. *S* is highly variable and it is difficult to estimate its actual uncertainty range. In

383   this study, we assume that $\delta S = 20\%$ (or $\Delta S = 12$ sr) according to a previous study (Müller et al., 2007). The light-

384   blue line in Figure B1 shows that the accumulative uncertainties in the aerosol backscatter due to ΔS using Eq. (B7)

385   and (B4) are close to the assumed 20% uncertainty for δS. $\delta\beta^S_A(r)$ is the largest error source in the PBL which is the

386   near range of the lidar. $\delta\beta^S_A(r)$ decreases with an increase in wavelength because of increasing $B(r)$. In other words,

387   $\delta\beta^S_A(r)$ is less sensitive to ΔS at longer wavelengths.

388   **B.5 Ozone error**

389   Similar to *S*, the ozone uncertainty affects only the transmittance term in Eqn. (A2) and its error propagation on aerosol

390   backscatter retrieval can be expressed as:

391   $$\delta\beta^{O3}_A(r) = 2\left[\frac{1}{B(r)} + 1\right]\Delta\alpha_{O3}(r)\Delta r. \qquad (B8)$$

392   $\delta\beta^{O3}_A(r)$ is proportional to the $\left[\frac{1}{B(r)} + 1\right]$ factor and ozone absorption uncertainty, meaning that $\delta\beta^{O3}_A(r)$ is smaller at

393   longer wavelengths due to larger aerosol scattering ratio and smaller ozone absorption. When Δr is specified at 22.5

Atmospheric
Measurement
Techniques
Discussions
Open Access
EGU

394   m, $\delta\beta_A^{O3}(r)$ is less than 0.3%. We still simulate the vertical accumulation of $\delta\beta_A^{O3}(r)$ using Eq. (B4). As noted earlier,

395   the systematic errors of the DIAL ozone measurement tend to accumulate while the random errors tend to cancel out.

396   The dominant error source for lidar measurements at the far range is typically the lidar signal detection noise, a type

397   of random error. Therefore, for purposes of estimation, we assume a 5% constant DIAL retrieval uncertainty primarily

398   covering the uncertainties due to ozone absorption cross section, non-ozone gas interference, and signal saturation

399   effect (Leblanc et al., 2018; Wang et al., 2017). As shown in Figure B1, the simulated aerosol retrieval uncertainty

400   due to ozone is relatively minor and is less than 5% at most altitudes.

401   In summary, the uncertainties in aerosol backscatter retrieval for the ozone lidar are controlled by ΔS at near

402   ranges (i. e., in the PBL) where the air is most turbid and are determined by both the lidar signal detection error and

403   inaccurate boundary value assumption at far ranges (higher than 7 km) where the air is typically clear. In the middle

404   range of the lidar measurement (PBL top – 7 km), the air density calculation error may become a significant error

405   source for aerosol retrieval and may have a comparable influence on the aerosol retrieval as the lidar signal

406   measurement error. Relative to the above four uncertainty sources, ozone DIAL retrieval error is relatively

407   unimportant especially in the lower altitudes where lidar SNR is large enough. All the uncertainty terms are affected

408   by the aerosol-to-molecular backscatter ratio, $B(r)$, which represents the relative importance of the aerosol component

409   in both extinction and backscatter processes. Based on the above uncertainty budget analysis, we conclude that the

410   RO$_3$QET lidar is capable of measuring aerosol profile reliably below 6 km with the current laser output power.

411

Acknowledgements

419

References

421   Ackermann, J. (1998). The extinction-to-backscatter ratio of tropospheric aerosol: A numerical study. *Journal of*

422   *atmospheric and oceanic technology*, *15*(4), 1043-1050.

423   Alvarez, R. J., Senff, C. J., Langford, A. O., Weickmann, A. M., Law, D. C., Machol, J. L., ... & Hardesty, R. M.

424   (2011). Development and application of a compact, tunable, solid-state airborne ozone lidar system for

425   boundary layer profiling. *Journal of Atmospheric and Oceanic Technology*, *28*(10), 1258-1272.

426   Ångström, A. (1929). On the atmospheric transmission of sun radiation and on dust in the air. *Geografiska Annaler*,

427   *11*(2), 156-166.

428   Browell, E. V., Ismail, S., and Shipley, S. T.: Ultraviolet DIAL measurements of O3 profiles in regions of spatially

429   inhomogeneous aerosols, Appl. Opt., 24, 2827-2836, 1985.

Atmospheric
Measurement
Techniques
Discussions

430   Browell, E. V., Fenn, M. A., Butler, C. F., Grant, W. B., Harriss, R. C., & Shipham, M. C. (1994). Ozone and aerosol
431   distributions in the summertime troposphere over Canada. *Journal of Geophysical Research: Atmospheres*,
432   *99*(D1), 1739-1755.

433   Burton, S. P., Ferrare, R. A., Hostetler, C. A., Hair, J. W., Rogers, R. R., Obland, M. D., ... & Froyd, K. D. (2012).
434   Aerosol classification using airborne High Spectral Resolution Lidar measurements–methodology and
435   examples. *Atmospheric Measurement Techniques*, *5*(1), 73-98.

436   Cattrall, C., Reagan, J., Thome, K., & Dubovik, O. (2005). Variability of aerosol and spectral lidar and backscatter
437   and extinction ratios of key aerosol types derived from selected Aerosol Robotic Network locations. *Journal*
438   *of Geophysical Research: Atmospheres*, *110*(D10).

439   De Young, R., Carrion, W., Ganoe, R., Pliutau, D., Gronoff, G., Berkoff, T., & Kuang, S. (2017). Langley mobile
440   ozone lidar: ozone and aerosol atmospheric profiling for air quality research. *Applied optics*, *56*(3), 721-730.

441   Eck, T. F., Holben, B. N., Reid, J. S., Dubovik, O., Smirnov, A., O'neill, N. T., ... & Kinne, S. (1999). Wavelength
442   dependence of the optical depth of biomass burning, urban, and desert dust aerosols. *Journal of Geophysical*
443   *Research: Atmospheres*, *104*(D24), 31333-31349.

444   Eisele, H., & Trickl, T. (2005). Improvements of the aerosol algorithm in ozone lidar data processing by use of
445   evolutionary strategies. *Applied optics*, *44*(13), 2638-2651.

446   Eloranta, E. E. (2005). High spectral resolution lidar. In *Lidar* (pp. 143-163). Springer, New York, NY.

447   Fernald, F. G. (1984). Analysis of atmospheric lidar observations: some comments. *Applied optics*, *23*(5), 652-653.

448   Fukuchi, T., Fujii, T., Cao, N., Nemoto, K., & Takeuchi, N. (2001). Tropospheric O3 measurement by simultaneous
449   differential absorption lidar and null profiling and comparison with sonde measurement. *Optical*
450   *Engineering*, *40*.

451   Gronoff, G., Robinson, J., Berkoff, T., Swap, R., Farris, B., Schroeder, J., ... & Adcock, E. E. (2019). A method for
452   quantifying near range point source induced O3 titration events using Co-located Lidar and Pandora
453   measurements. *Atmospheric Environment*, *204*, 43-52.

454   Grund, C. J., & Eloranta, E. W. (1991). University of Wisconsin high spectral resolution lidar. *Optical Engineering*,
455   *30*(1), 6-13.

456   Groß, S., Esselborn, M., Weinzierl, B., Wirth, M., Fix, A., & Petzold, A. (2013). Aerosol classification by airborne
457   high spectral resolution lidar observations. *Atmospheric chemistry and physics*, *13*(5), 2487-2505.

458   Hair, J. W., Hostetler, C. A., Cook, A. L., Harper, D. B., Ferrare, R. A., Mack, T. L., ... & Hovis, F. E. (2008). Airborne
459   high spectral resolution lidar for profiling aerosol optical properties. *Applied optics*, *47*(36), 6734-6752.

460   Hurst, D. F., Hall, E. G., Jordan, A. F., Miloshevich, L. M., Whiteman, D. N., Leblanc, T., ... & Oltmans, S. J. (2011).
461   Comparisons of temperature, pressure and humidity measurements by balloon-borne radiosondes and frost
462   point hygrometers during MOHAVE-2009. *Atmospheric Measurement Techniques*, *4*(12), 2777-2793.

463   Immler, F. (2003). A new algorithm for simultaneous ozone and aerosol retrieval from tropospheric DIAL
464   measurements. *Applied Physics B*, *76*(5), 593-596.

465   Kempfer, U., Carnuth, W., Lotz, R., & Trickl, T. (1994). A wide-range ultraviolet lidar system for tropospheric ozone
466   measurements: Development and application. *Review of scientific instruments*, *65*(10), 3145-3164.

467   Klein, A., Ravetta, F., Thomas, J. L., Ancellet, G., Augustin, P., Wilson, R., ... & Pelon, J. (2019). Influence of vertical

468   mixing and nighttime transport on surface ozone variability in the morning in Paris and the surrounding

469   region. *Atmospheric environment*, *197*, 92-102.

470   Klett, J. D. (1981). Stable analytical inversion solution for processing lidar returns. *Applied optics*, *20*(2), 211-220.

471   Klett, James D. "Lidar inversion with variable backscatter/extinction ratios." *Applied optics* 24.11 (1985): 1638-1643.

472   Kovalev, V. A., & Eichinger, W. E. (2004). *Elastic lidar: theory, practice, and analysis methods*. John Wiley & Sons.

473   Kovalev, V. A., & Moosmüller, H. (1994). Distortion of particulate extinction profiles measured with lidar in a two-

474   component atmosphere. *Applied optics*, *33*(27), 6499-6507.

475   Kovalev, V. A., & McElroy, J. L. (1994). Differential absorption lidar measurement of vertical ozone profiles in the

476   troposphere that contains aerosol layers with strong backscattering gradients: a simplified version. *Applied

477   optics*, *33*(36), 8393-8401.

478   Kuang, S., Burris, J. F., Newchurch, M. J., Johnson, S., and Long, S.: Differential Absorption Lidar to Measure

479   Subhourly Variation of Tropospheric Ozone Profiles, IEEE Transactions on Geoscience and Remote Sensing,

480   49, 557-571, 10.1109/TGRS.2010.2054834, 2011.

481   Kuang, S., Newchurch, M. J., Burris, J., and Liu, X.: Ground-based lidar for atmospheric boundary layer ozone

482   measurements, Appl. Opt., 52, 3557-3566, 10.1364/AO.52.003557, 2013.

483   Kuang, S., Newchurch, M. J., Johnson, M. S., Wang, L., Burris, J., Pierce, R. B., ... & Warneke, C. (2017).

484   Summertime tropospheric ozone enhancement associated with a cold front passage due to stratosphere-to-

485   troposphere transport and biomass burning: Simultaneous ground-based lidar and airborne measurements.

486   *Journal of Geophysical Research: Atmospheres*, *122*(2), 1293-1311.

487   Langford, A. O., Alvarez, I. I., Raul, J., Kirgis, G., Senff, C. J., Caputi, D., ... & McNamara, M. E. (2019).

488   Intercomparison of lidar, aircraft, and surface ozone measurements in the San Joaquin Valley during the

489   California Baseline Ozone Transport Study (CABOTS). *Atmospheric Measurement Techniques*, *12*(3), 1889-

490   1904.

491   Leblanc, T., Sica, R. J., van Gijsel, J. A. E., Godin-Beekmann, S., Haefele, A., Trickl, T., Payen, G., and Gabarrot, F.:

492   Proposed standardized definitions for vertical resolution and uncertainty in the NDACC lidar ozone and

493   temperature algorithms – Part 1: Vertical resolution, Atmos. Meas. Tech., 9, 4029-4049, 10.5194/amt-9-

494   4029-2016, 2016a.

495   Leblanc, T., Sica, R.J., Van Gijsel, J.A., Godin-Beekmann, S., Haefele, A., Trickl, T., Payen, G. and Liberti, G., 2016.

496   Proposed standardized definitions for vertical resolution and uncertainty in the NDACC lidar ozone and

497   temperature algorithms–Part 2: Ozone DIAL uncertainty budget. Atmospheric Measurement Techniques,

498   9(8), pp.4051-4078, 2016b.

499   Leblanc, T., Brewer, M. A., Wang, P. S., & Granados Muñoz, M. J. (2018). Validation of the TOLNet lidars: the

500   Southern California Ozone Observation Project (SCOOP). *Atmospheric measurement techniques*, *11*, 6137-

501   6162.

502   McDermid, I. S., Beyerle, G., Haner, D. A., & Leblanc, T. (2002). Redesign and improved performance of the
503   tropospheric ozone lidar at the Jet Propulsion Laboratory Table Mountain Facility. *Applied optics*, *41*(36),
504   7550-7555.

505   Mishchenko, M. I., Travis, L. D., Kahn, R. A., & West, R. A. (1997). Modeling phase functions for dustlike
506   tropospheric aerosols using a shape mixture of randomly oriented polydisperse spheroids. *Journal of
507   Geophysical Research: Atmospheres*, *102*(D14), 16831-16847.

508   Müller, D., Ansmann, A., Mattis, I., Tesche, M., Wandinger, U., Althausen, D., & Pisani, G. (2007). Aerosol-type-
509   dependent lidar ratios observed with Raman lidar. *Journal of Geophysical Research: Atmospheres*,
510   *112*(D16).

511   Newell, R. E., Thouret, V., Cho, J. Y., Stoller, P., Marenco, A., & Smit, H. G. (1999). Ubiquity of quasi-horizontal
512   layers in the troposphere. *Nature*, *398*(6725), 316.

513   Papayannis, A. D., Porteneuve, J., Balis, D., Zerefos, C., & Galani, E. (1999). Design of a new DIAL system for
514   tropospheric and lower stratospheric ozone monitoring in Northern Greece. *Physics and Chemistry of the
515   Earth, Part C: Solar, Terrestrial & Planetary Science*, *24*(5), 439-442.

516   Proffitt, M. H., & Langford, A. O. (1997). Ground-based differential absorption lidar system for day or night
517   measurements of ozone throughout the free troposphere. *Applied optics*, *36*(12), 2568-2585.

518   Reid, J. S., Kuehn, R. E., Holz, R. E., Eloranta, E. W., Kaku, K. C., Kuang, S., ... & Atwood, S. A. (2017). Ground-
519   based High Spectral Resolution Lidar observation of aerosol vertical distribution in the summertime
520   Southeast United States. *Journal of Geophysical Research: Atmospheres*, *122*(5), 2970-3004.

521   Russell, P. B., Swissler, T. J., & McCormick, M. P. (1979). Methodology for error analysis and simulation of lidar
522   aerosol measurements. *Applied Optics*, *18*(22), 3783-3797.

523   Strawbridge, K. B., Travis, M. S., Firanski, B. J., Brook, J. R., Staebler, R., & Leblanc, T. (2018). A fully autonomous
524   ozone, aerosol and nighttime water vapor lidar: a synergistic approach to profiling the atmosphere in the
525   Canadian oil sands region. *Atmospheric Measurement Techniques*, *11*(12), 6735-6759.

526   Sullivan, J. T., McGee, T. J., Sumnicht, G. K., Twigg, L. W., & Hoff, R. M. (2014). A mobile differential absorption
527   lidar to measure sub-hourly fluctuation of tropospheric ozone profiles in the Baltimore–Washington, DC
528   region. *Atmospheric Measurement Techniques*, *7*(10), 3529-3548.

529   Uchino, O., & Tabata, I. (1991). Mobile lidar for simultaneous measurements of ozone, aerosols, and temperature in
530   the stratosphere. *Applied optics*, *30*(15), 2005-2012.

531   Wang, L., Newchurch, M. J., Alvarez II, R. J., Berkoff, T. A., Brown, S. S., Carrion, W., DeYoung R. J., Johnson, B.
532   J., Ganoe, R., Gronoff, G., Kirgis G., Kuang, S., Langford, A. O., Leblanc T., McDuffie E. E., McGee, T. J.,
533   Pliutau, D., Senff, C. J., Sullivan, J. T., Sumnicht, G., Twigg, L. W., & Weinheimer, A. J. (2017). Quantifying
534   TOLNet ozone lidar accuracy during the 2014 DISCOVER-AQ and FRAPPE campaigns. *Atmospheric
535   Measurement Techniques*, 10(10), 3865-3876.

536

Atmospheric
Measurement
Techniques
Discussions

EGU

Open Access

537
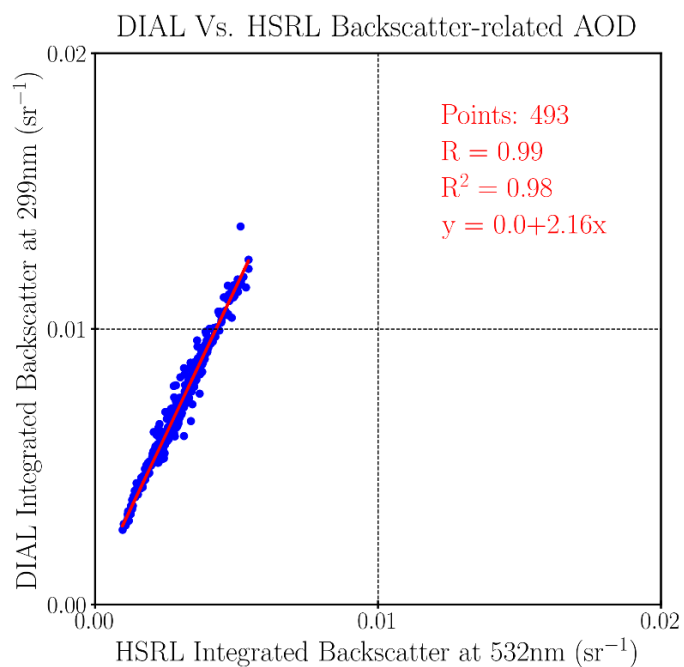
Figure 1. Regression of the ozone lidar and HSRL derived integrated aerosol backscatter between 0.4 and 6 km asl

using the best least-square fit resulting in a backscatter color ratio of 1.34 for 299–532-nm for four cases in 2013. All

data was taken at Huntsville, AL, USA, during the summertime 2013.

541

542
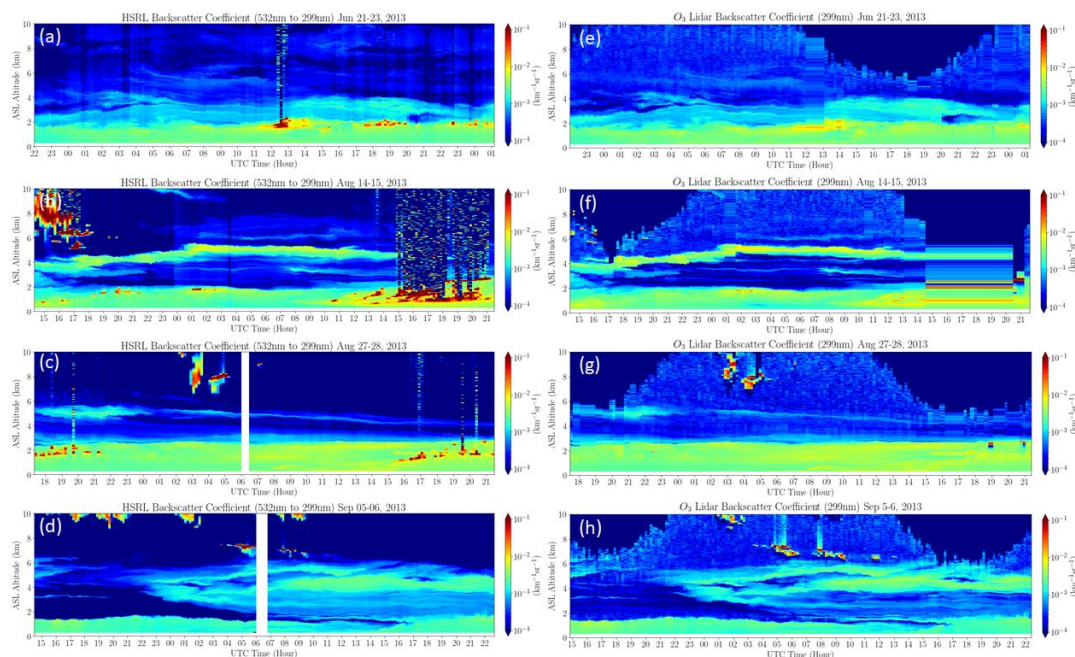
Figure 2. HSRL-converted aerosol backscatter coefficients (a, b, c, d) compared to the RO$_3$QET lidar derived aerosol backscatter coefficients at 299 nm (e, f, g, h), with 10-min temporal resolution and 30-m vertical resolution. The data was taken from 21–23 June (a, e), 14-15 August (b, f), 27–28 August (c, g), and 5–6 September (d, h) 2013. The HSRL-converted aerosol backscatter coefficients are scaled from the original retrievals at 532 nm to 299 nm using Eq. (1) and å$_\beta$=1.34.

Atmospheric
Measurement
Techniques
Discussions

Open Access

EGU
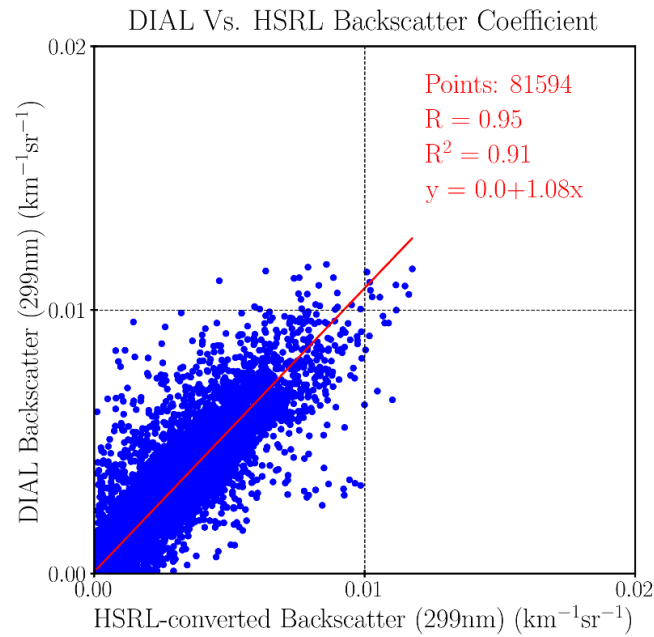
549

550   Figure 3. Regression of the ozone lidar measured and HSRL-converted aerosol backscatter coefficients (interpolated

551   at 299 nm with $å_\beta$=1.34) with 30-m vertical resolution and 10-min temporal resolution.

552

Atmospheric
Measurement
Techniques
Discussions

Open Access

EGU
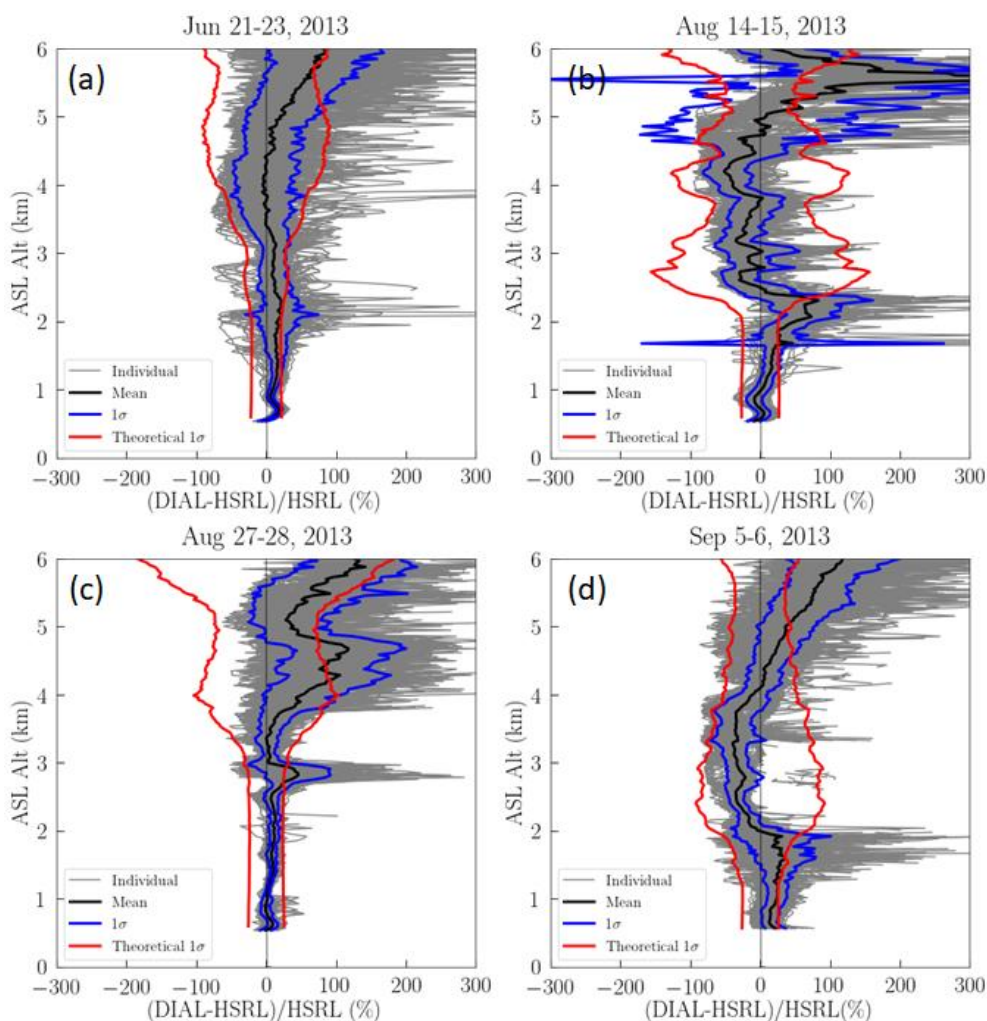
Figure 4. Relative differences between the RO₃QET and HSRL-converted aerosol backscatter measurements, (RO₃QET-HSRL)/HSRL, made from (a) 21-–23 June, (b) 14-–15 August, (c) 27–28 August, and (d) 5–6 September, 2013. The gray and black lines represent the differences for the 10-min individual aerosol backscatter profiles and their mean, respectively. The blue lines represent the actual 1 σ of the differences compared to the theoretical 1 σ (red lines) of the RO₃QET lidar aerosol measurement.

560
561   (a)   (b)
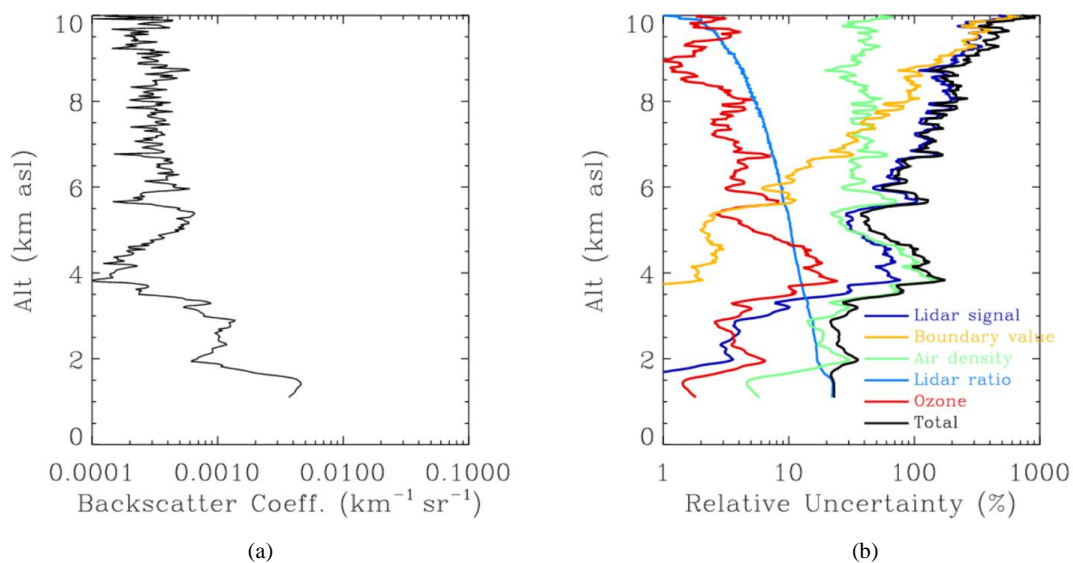
562   Figure B1. An example of (a) aerosol backscatter profile retrieved from a 10-min ozone lidar data at about 8:30 UTC

563   on 22 June 2013 and (b) its retrieval error budget for different uncertainty sources. The lidar data was from the

564   Channel-3 receiving system which covers most of the measurement altitude range and was arbitrarily chosen for a

565   cloud-free condition.

566